



Cite this: DOI: 10.1039/d5lf00395d

# From egg-shell to uniform distribution of platinum by atomic layer deposition on mesoporous alumina spheres: experiments and modeling

Christine Gonsalves,<sup>a</sup> Jänis Järvillehto,<sup>ab</sup> Saeed Saedy,<sup>b</sup> Jorge A. Velasco,<sup>a</sup> Thomas Grehl,<sup>c</sup> Philipp Brüner,<sup>c</sup> Niko Heikkinen,<sup>d</sup> Juha Lehtonen,<sup>d</sup> J. Ruud van Ommen<sup>b</sup> and Riikka L. Puurunen<sup>\*,a</sup>

Uniform material distribution by atomic layer deposition (ALD) inside porous materials is needed in multiple applications, including batteries and catalysis. Attaining this uniformity is not trivial, diffusion within the porous network being one of the main limiting factors. This work used a fluidized bed atmospheric ALD reactor to coat millimeter-size mesoporous alumina spheres with platinum, using the process based on (methylcyclopentadienyl)trimethylplatinum [MeCpPtMe<sub>3</sub>] and oxygen. Using different exposure times and five reaction cycles, materials with platinum loading up to ~4 wt% were prepared. The growth per cycle, expressed as average areal number density, was approximately 0.1 Pt atoms per nm<sup>2</sup>. Cross-sectional analysis done using low-energy ion scattering indicated that with increasing exposure time, platinum distribution evolved from egg-shell to macroscopic uniform distribution through the particles. Diffusion-reaction modeling was done to support the experiments and showed a saturation of the Pt weight loading after uniform distribution. This work shows that it is possible to get a uniform distribution of platinum through mesoporous particles with an aspect ratio on the order of 100 000 : 1, when the ALD process is properly optimized.

Received 18th December 2025,  
Accepted 1st April 2026

DOI: 10.1039/d5lf00395d

rsc.li/RSCApplInter

## 1 Introduction

Atomic layer deposition (ALD) is a technique that is based on sequential and self-limiting gas–solid surface reactions,<sup>1,2</sup> widely used for fabricating uniform thin films on flat substrates and conformal coatings in complex, high-aspect-ratio structures.<sup>1,3</sup> In principle, ALD can enable conformal growth on any surface, regardless of geometry, since the reactions occur by chemisorption. Over a thousand ALD chemistries have been developed, reflecting its broad application potential.<sup>4,5</sup> ALD is attractive for coating particles,<sup>3,6–8</sup> with growing applications in heterogeneous thermocatalysis,<sup>9,10</sup> battery electrodes,<sup>11</sup> fuel cells,<sup>12</sup> LED phosphors<sup>13,14</sup> and drug delivery systems.<sup>15</sup> Recently, a review article overviewed ~800 scientific articles reporting ALD on particulate materials.<sup>16</sup>

ALD is attractive for coating porous materials with expensive noble metals such as platinum, as it potentially provides precise particle size control and efficient use of precursors.<sup>17</sup> Platinum is a critical catalyst in applications such as fuel cells,<sup>12,18,19</sup> where it facilitates the oxygen reduction and hydrogen oxidation reactions,<sup>20</sup> and in hydrogenation processes,<sup>21,22</sup> where it activates molecular hydrogen. Deposition of platinum by ALD has been demonstrated on a variety of substrates, including nonporous anodic alumina membranes<sup>23–27</sup> and porous nanotubes,<sup>28–30</sup> and trench-type high-aspect-ratio geometries.<sup>31–34</sup> Platinum ALD has been reported to date<sup>4,5,16</sup> using a handful of precursors: platinum(II) acetylacetonate [Pt(acac)<sub>2</sub>],<sup>35</sup> dimethyl(η<sup>4</sup>-cyclohexa-1,5-diene)platinum [PtMe<sub>2</sub>(η<sup>4</sup>-cyclohexa-1,5-diene)],<sup>36</sup> dimethyl(*N,N*-dimethyl-3-butene-1-amine-*N*)platinum (DDAP, [C<sub>8</sub>H<sub>19</sub>NPt]),<sup>37,38</sup> and (methylcyclopentadienyl)trimethylplatinum [MeCpPtMe<sub>3</sub>].<sup>39–43</sup> Out of these, MeCpPtMe<sub>3</sub> is the most commonly used Pt precursor due to its stability and high volatility,<sup>16,32</sup> and has been used in this work.

Several experimental studies have investigated the macroscopic distribution of various ALD-deposited materials on porous substrates. Table 1 summarizes earlier work on porous spheres. While most studies<sup>44–46</sup> report only an eggshell-type coating, there are also reports where uniform coating (*i.e.*, through particle coating) is seen.<sup>47–49</sup> Elam

<sup>a</sup> Department of Chemical and Metallurgical Engineering, Aalto University, P.O. Box 16100, FI-00076 AALTO, Finland. E-mail: christine.gonsalves@aalto.fi, riikka.puurunen@aalto.fi

<sup>b</sup> Department of Chemical Engineering, Process and Product Technology Institute, Delft University of Technology, Van der Maasweg 9, 2629 HZ Delft, The Netherlands

<sup>c</sup> IONTOF GmbH, Munster, Germany

<sup>d</sup> VTT Technical Research Center Finland, P.O. Box 1000, FI-02044 VTT, Finland





Table 1 Summary of ALD-based metal distribution on porous spheres in the literature<sup>a</sup>

| ALD grown material             | Substrate material   | ALD reactants  | ALD process |            | Exposure                           |            | Average support particle diameter 2R (mm) | Average pore diameter (nm) | Aspect ratio <sup>b</sup> | Penetration depth (μm) | References |
|--------------------------------|--|--|-------------|------------|------------------------------------|------------|---|----------------------------|---------------------------|------------------------|------------|
|                                |  |  | Temp. (°C)  | Cycles (—) | time/purge/exposure time/purge (s) | R          |   |                            |                           |                        |            |
| Al <sub>2</sub> O <sub>3</sub> | Co-Pt/TiO <sub>2</sub>   | Al(CH <sub>3</sub> ) <sub>3</sub> , H <sub>2</sub> O               | 150         | 30         | 10/80/10/180 <sup>c</sup>          | 0.4        | 29  | 6897:1                     | 9.6                       | 4.8%                   | 44         |
| NiO                            | Al <sub>2</sub> O <sub>3</sub>   | NiCp <sub>2</sub> , O <sub>2</sub>                                 | 260         | 50         | 200 + 30/—/10 + 30/— <sup>d</sup>  | 1.1        | 11.6                                      | 47 414:1                   | 15                        | 2.8%                   | 45         |
| Pd                             | Closed macroporous <sup>e</sup> Al <sub>2</sub> O <sub>3</sub>             | Pd(hfac) <sub>2</sub> , formalin                                   | 220         | 300        | 0.5 + 15/10/1 + 15/15 <sup>f</sup> | 2.5        | 10  | 125 000:1                  | 16                        | 1.3%                   | 46         |
| Pd                             | Randomly dispersed macroporous <sup>g</sup> Al <sub>2</sub> O <sub>3</sub> | Pd(hfac) <sub>2</sub> , formalin                                   | 220         | 300        | 0.5 + 15/10/1 + 15/15 <sup>f</sup> | 2.8        | 11  | 127 273:1                  | 16                        | 1.1%                   | 46         |
| Al <sub>2</sub> O <sub>3</sub> | Silica gel: Silicycle S10040M  | Al(CH <sub>3</sub> ) <sub>3</sub> , H <sub>2</sub> O               | 150         | 9          | 90/180/90/180                      | 0.1        | 30  | 1667:1                     | 45                        | 100%                   | 47         |
| ZnO                            | Silicycle S10040M or fumed silica (Ineos USA LLC)                          | Zn(C <sub>2</sub> H <sub>2</sub> ) <sub>2</sub> , H <sub>2</sub> O | 200         | 3          | 180/540/—/— <sup>h</sup>           | 0.075      | 30 <sup>i</sup>                           | 1250:1 (Silicycle)         | 45                        | 100%                   | 58         |
| Pt                             | Silica gel <sup>j</sup>  | MeCpPtMe <sub>3</sub> , O <sub>2</sub>                             | 325         | 10         | —/—/—/— <sup>k</sup>               | 0.03–0.075 | 6   | 6250:1                     | 45                        | 100%                   | 59         |
| RuO <sub>2</sub>               | Al <sub>2</sub> O <sub>3</sub>   | Ru(EtCp) <sub>2</sub> , O <sub>2</sub>                             | 315         | 50         | 180/—/10 + 30/— <sup>l</sup>       | 1          | 11.6                                      | 43 103:1                   | 45                        | 100%                   | 48         |
| Al <sub>2</sub> O <sub>3</sub> | Nanocomposite polymer beads <sup>m</sup>                                   | Al(CH <sub>3</sub> ) <sub>3</sub> , H <sub>2</sub> O               | 150         | 250        | 10/—/—/— <sup>n</sup>              | 1.5        | 3000                                      | 250:1                      | 45                        | 100%                   | 49         |
| TiO <sub>2</sub>               | Nanocomposite polymer beads <sup>m</sup>                                   | TiCl <sub>4</sub> , H <sub>2</sub> O                               | 250         | 500        | 10/—/—/— <sup>n</sup>              | 1.5        | 3000                                      | 250:1                      | 45                        | 100%                   | 49         |
| ZnO                            | Nanocomposite polymer beads <sup>m</sup>                                   | Zn(C <sub>2</sub> H <sub>2</sub> ) <sub>2</sub> , H <sub>2</sub> O | 175         | 250        | 10/—/—/— <sup>n</sup>              | 1.5        | 3000                                      | 250:1                      | 45                        | 100%                   | 49         |

<sup>a</sup> Authors' interpretation of the literature data. <sup>b</sup> Aspect ratio was calculated as the ratio of particle radius *R* to pore diameter. <sup>c</sup> This ALD process was done using a Picosun R-200 reactor with stop flow deposition and purge cycles. The stop-flow cycle had a 0.7 s precursor pulse and 9.3 s equilibrium time. <sup>d</sup> The metal precursor injection time was 200 s and the substrate was exposed to the injected precursor for 30 s. Oxygen precursor was injected 10 s and remained for 30 s. The purge times are not reported. <sup>e</sup> This support had spherical and micrometer-sized macropores that communicated only through mesopores. <sup>f</sup> The ALD cycle consisted of a 0.5 s pulse of Pd(hfac)<sub>2</sub>, 15 s of exposure, and a 10 s Ar purge, followed by a 1 s pulse of formalin, 15 s of exposure, and again a 15 s purge with Ar. <sup>g</sup> This support had interconnected randomly dispersed macropores. <sup>h</sup> 180 s exposure times and 540 s purge times were used. <sup>i</sup> Silicycle support's pore diameter was 30 nm. <sup>j</sup> The results are included assuming the particles were spherical, although the shape was explicitly mentioned in the article. <sup>k</sup> Exposure and purge times are not directly reported. The Pt precursor dose was on the order of 200 s. <sup>l</sup> Metal precursor was injection time was 180 s. Then, O<sub>2</sub> was injected into the reactor for 10 s and the sample was subsequently exposed to O<sub>2</sub> for 30 s. Between injections of each precursor, the reactor was purged with nitrogen. The purge times are not reported. <sup>m</sup> Total porosity ~90%; three-dimensional interconnected microcellular structure with voids 10 ± 3 μm and windows 3 ± 1 μm, typical of high internal phase emulsion polymerization. The window dimensions were taken as the basis for the aspect ratio calculation. <sup>n</sup> The second reactant's exposure time and the purge times are not reported. <sup>o</sup>

*et al.*<sup>47</sup> showed that progressively increasing the exposure (partial pressure  $\times$  time) led to increasing penetration upto uniform coating for a  $\text{Al}(\text{CH}_3)_3/\text{H}_2\text{O}$  ALD process with a 90 s precursor exposure time in porous silica particles (aspect ratio 1667:1, calculated as the ratio of particle radius to average pore diameter). To date, the highest aspect ratio for which uniform coating on a porous sphere has been reported is 43 103:1, done using a  $\text{Ru}(\text{EtCp})_2/\text{O}_2$  ALD process on alumina spheres with a 180 s precursor exposure time.<sup>48</sup>

To better understand and predict film conformality in challenging geometries, various models including analytical,<sup>50</sup> diffusion–reaction,<sup>51–54</sup> ballistic transport–reaction,<sup>53,55</sup> and Monte-Carlo<sup>3</sup> models have been developed to describe ALD growth in trenches, holes, and porous materials. For example, the analytical Gordon *et al.* model<sup>50</sup> showed that the penetration depth within a hole for Knudsen diffusion conditions (*i.e.* Knudsen number  $\gg 1$ , where Knudsen number is the ratio of the gas mean free path to a characteristic length scale) is proportional to the square root of the precursor exposure time.<sup>50</sup> Recently, a diffusion–reaction model<sup>56</sup> was adapted for porous particles in the shape of slabs, cylinders and spheres, where reactant transport initiates at the particle's outer surface and proceeds through a tortuous pathway toward the center, with the effective diffusion coefficient governing diffusion throughout the particle.<sup>56</sup> This model shows that spherical particles require less reactant exposure for full surface saturation than slabs or cylinders of the same size due to multidimensional reactant diffusion propagation along three radial directions (spheres require about one-third of the exposure required to saturate slabs).<sup>56,57</sup>

The goal of this work is to characterize ALD growth of platinum on mesoporous alumina spheres in a fluidized bed reactor at atmospheric pressure using the commonly used (trimethyl)methylcyclopentadienylplatinum(IV) reactant. We show that systematically increasing precursor exposure leads to increasing Pt penetration depth, from egg-shell to uniform distribution; on porous spheres up to 2.5 mm diameter with an aspect ratio on the order of 100 000:1. These experimental results are then compared with predictions from a diffusion–reaction model for spheres.<sup>56</sup> The model predictions align with the experiments, assuming a low precursor sticking coefficient.

## 2 Methods

### 2.1 Materials

Porous alumina spheres from SASOL Limited were used as the ALD support. The diameters were 1.0 mm (alumina spheres 1.0/160 prod. 610110), 1.8 mm (alumina spheres 1.8/210, prod. 604130) and 2.5 mm (alumina spheres 2.5/210 prod. 608114). The reactants used were: (trimethyl)methylcyclopentadienylplatinum(IV),  $\text{MeCpPtMe}_3$  (99%) from Strem Chemicals Inc., and synthetic air (Linde) nitrogen ( $\text{N}_2$ , 99.999%, Linde) was used as the inert carrier gas.

### 2.2 Platinum ALD

Platinum ALD was done at atmospheric pressure in a fluidized bed reactor with a process temperature of 110 °C. The fluidized-bed ALD reactor used in this study has been described in detail elsewhere;<sup>60,61</sup> a schematic is provided in the SI (Fig. S2). The process conditions were similar to those reported by Grillo *et al.*<sup>60</sup> The Pt precursor was placed in a stainless steel bubbler and was heated to 70 °C. The process consisted of the steps:  $\text{MeCpPtMe}_3$  exposure (duration from 180 s to 1440 s), purge I (600 s), synthetic air exposure (600 s), purge II (600 s). Parameters varied during the experiments are in Table 2. The alumina spheres were mixed with glass beads of 120–150  $\mu\text{m}$  diameter. Each run used 10 grams of glass beads and 0.25 grams of alumina spheres for each diameter of 1.0 mm, 1.8 mm, and 2.5 mm. Given that the particle mixing time in the fluidized bed ( $\sim 1$  s) is significantly shorter than the precursor pulse time, each particle is expected to experience a uniform time-averaged concentration, promoting a homogeneous coating across the batch.<sup>16,62,63</sup> In the experiments conducted, a flow rate of  $11 \text{ min}^{-1}$  (normal liter per second at 1 atm and 20 °C) was used, resulting in a fluidization velocity of approximately  $3.4 \text{ cm s}^{-1}$ . Detailed conditions for fluidization are in the SI (section S1.4).

Before ALD, the glass beads for the sample mixture were washed with diluted isopropanol ( $\sim 20\%$ ), and after that, with diluted nitric acid ( $\sim 10\%$ ). Four samples of  $\text{Pt}/\text{Al}_2\text{O}_3$  were obtained by varying the  $\text{MeCpPtMe}_3$  pulse time (180, 360, 720, and 1440 s) while the oxidizer's pulse time was kept constant at 600 s; five cycles of ALD were done for all samples.

**Table 2** Varied flows used in the experimental setup (total flow was constant:  $11 \text{ min}^{-1}$ ). One cycle consisted of the following steps:  $\text{MeCpPtMe}_3$  exposure, purge I, synthetic air exposure, purge II

| Step                         | $\dot{V}_{\text{N}_2, \text{purge I}}^a$<br>L $\text{min}^{-1}$ | $\dot{V}_{\text{N}_2, \text{bubbler}}^b$<br>L $\text{min}^{-1}$ | $\dot{V}_{\text{N}_2, \text{purge II}}^c$<br>L $\text{min}^{-1}$ | $\dot{V}_{\text{N}_2, \text{makeup}}^d$<br>L $\text{min}^{-1}$ | $\dot{V}_{\text{air}}^e$<br>L $\text{min}^{-1}$ |
|------------------------------|---|---|--|--|---|
| $\text{MeCpPtMe}_3$ exposure | 0   | 0.4   | 0  | 0.6  | 0   |
| Purge I                      | 0.8   | 0   | 0  | 0.2  | 0   |
| Synthetic air exposure       | 0   | 0   | 0  | 0  | 1   |
| Purge II                     | 0   | 0   | 0.8  | 0.2  | 0   |

<sup>a</sup>  $\dot{V}_{\text{N}_2, \text{purge I}}$  is the nitrogen volume flow bypassing the  $\text{MeCpPtMe}_3$  bubbler. <sup>b</sup>  $\dot{V}_{\text{N}_2, \text{bubbler}}$  is the nitrogen volume flow through the  $\text{MeCpPtMe}_3$  bubbler. <sup>c</sup>  $\dot{V}_{\text{N}_2, \text{purge II}}$  is the nitrogen volume flow through the air line. <sup>d</sup>  $\dot{V}_{\text{N}_2, \text{makeup}}$  is the nitrogen makeup volume flow. <sup>e</sup>  $\dot{V}_{\text{air}}$  is the air volume flow.



### 2.3 Nitrogen physisorption

The surface area, total pore volume, and pore size of the spheres was determined by nitrogen physisorption. The measurements were made with a Micromeritics Tristar II 3020 instrument. The specific surface area was determined using the Brunauer–Emmett–Teller (BET)<sup>64</sup> method. Total pore volume and the pore size distribution were determined by the Barrett–Joyner–Halenda (BJH)<sup>65</sup> method.

### 2.4 Inductively coupled plasma-optical emission spectrometry

The average metal weight loading of platinum on the porous alumina spheres was determined using a PerkinElmer Optima 8000 inductively coupled plasma-optical emission spectrometer. In the inductively coupled plasma-optical emission spectrometry (ICP-OES) analysis, each particle size fraction was analyzed separately. Approximately 30 mg of the sample was digested in a microwave for 60 minutes in a mixture of 4.5 ml of 30% hydrochloric acid and 1.5 ml of 65% nitric acid. The samples were then diluted to 50 ml with purified water before the analysis with ICP-OES 8000.

### 2.5 Average areal number density calculation

From experimental values of average metal weight loadings (in this work determined from ICP-OES), the average number of metal atoms per surface area of the support, referred to as areal number density  $c_M$  ( $\text{nm}^{-2}$ ) is calculated as<sup>2,8</sup>

$$c_M = \frac{w_M N_0 m_t}{M_M S m_s} \quad (1)$$

Here,  $w_M$  is the weight fraction of the metal,  $N_0$  ( $\text{mol}^{-1}$ ) is Avogadro's constant,  $M_M$  ( $\text{g}_{\text{metal}} \text{mol}^{-1}$ ) is the molar mass of the metal,  $S$  ( $\text{m}^2 \text{g}_{\text{support}}^{-1}$ ) is the specific surface area of the support,  $m_t$  ( $\text{g}_{\text{sample}}$ ) is the total mass of the sample including the amount of the deposited material, and  $m_s$  ( $\text{g}_{\text{support}}$ ) is the mass of the original support. An example of the average areal number density calculation is in section S2.2 of the SI. Additionally, for the largest sphere size (2.5 mm), we calculated the areal number density on the coated area, based on the coated volume fraction  $\phi_{\text{coat}}$  (Table S2 in the SI).

### 2.6 CO pulsed chemisorption

CO pulsed chemisorption was used to analyse platinum crystallite size and dispersion of ALD coated Pt/ $\text{Al}_2\text{O}_3$  spheres of diameter 2.5 mm. An AutoChem-III 2930 tool (Micromeritics Instrument Corporation) with an external Cirrus™ 3 mass spectrometer (MS; MKS Instruments) was used.

In a U-shaped reactor tube, approximately 60 mg of sample was placed and diluted with 300 mg of silicon carbide, SiC (Thermo Scientific, 46 grit). The sample was then dried by heating to 200 °C (ramp rate: 10 °C  $\text{min}^{-1}$ ) for 1 hour in a helium (He, Woikoski, 99.9995%) flow of 50  $\text{ml min}^{-1}$  and then cooled to 35 °C after drying. Flow was then changed from He to a gas mixture of  $\text{H}_2/\text{Ar}$  (10%  $\text{H}_2$  in Ar, Air products, 9.99%) with a flow rate of 50  $\text{ml min}^{-1}$ . The

sample was then reduced in a gas mixture of  $\text{H}_2/\text{Ar}$  while heating to 400 °C (ramp rate: 10 °C  $\text{min}^{-1}$ ). The hold time at 400 °C was 0.5 hour. After reduction, flow was changed to He to remove chemisorbed hydrogen (flow rate 50  $\text{ml min}^{-1}$ ), and after 0.5 hour, the sample was cooled to 35 °C.

Then, pulse chemisorption of CO was carried out. In total, 25 pulses of CO/He (10% CO in He, Air products, 9.998%) were dosed to the sample using a loop. The physically calibrated loop volume was 0.5185  $\text{cm}^3$ . The temperature of the loop and the equipment's lines was 110 °C. The thermal conductivity detector (TCD) and mass spectrometer,  $m/z = 28$  (CO) signals were used to estimate the amount of CO adsorbed. Pt dispersion and platinum crystallite particle size were calculated based on the CO consumption, assuming hemispherical Pt particles and an adsorption stoichiometry of 1. The equations used to calculate metal dispersion and hemispherical crystallite size are provided in the SI (section S1.3).

### 2.7 Low-energy ion scattering

Low-energy ion scattering (LEIS) surface spectroscopy was performed on the inner surfaces of the samples using an IONTOF Qtac 100 low-energy ion scattering spectrometer. The purpose was to study the propagation of the ALD Pt coating from the outer surface towards the center of the porous alumina spheres. Before analysis, the spheres were mechanically cut approximately in half with scissors to obtain cross-sections, and the samples were cleaned in the ultra-high vacuum of the instrument by exposure to atomic oxygen extracted from a remote plasma source.  $^4\text{He}^+$  was used as the analysis ion (3 keV, 5.2 nA) with an acquisition time of 1200 s, scanning over an analysis area of  $2.8 \times 2.8 \text{ mm}^2$  using a  $256 \times 256$  pixel raster. The resulting ion dose density was  $4.8 \times 10^{14}$  ions per  $\text{cm}^2$ . The  $\text{PtO}_2$  surface coverage was quantified *via* a  $\text{PtO}_2$  powder reference sample (Sigma Aldrich, CAS: 1314-15-4). The horizontal line scans through the center of the alumina spheres are averaged over 16 pixels in the vertical direction. Line scans are plotted with 11 pt adjacent averaging.

### 2.8 Diffusion–reaction model

A diffusion–reaction model was used to compare the saturation profiles obtained experimentally with those predicted by simulations. The model equations are based on the diffusion–reaction model for porous spheres by Heikkinen *et al.*<sup>56</sup> and the model by Ylilammi *et al.*<sup>51,52</sup> The main equations are described in this section, and some additional equations are shown in the SI (section S1.1). The set of equations was solved using a Python-based script.<sup>66</sup> This model assumes uniform porosity, tortuosity, and pore size across the entire particle. It takes the precursor partial pressure at the entrance  $p_{A0}$  (related to the reactant number density  $n_{A0}$  through the ideal gas equation) as a constant value, and describes reactant transport through diffusion from the outer surface towards the core of a sphere of radius  $R$ :



$$\frac{\partial n_A(r,t)}{\partial t} = D_{\text{eff}} \frac{\partial^2 n_A(r,t)}{\partial r^2} + D_{\text{eff}} \frac{2}{r} \frac{\partial n_A(r,t)}{\partial r} - \bar{s} \cdot \left[ \frac{1}{4} \bar{v}_A \cdot c \cdot n_A(r,t) \cdot [1 - \theta(r,t)] - P_d \cdot q \cdot \theta(r,t) \right] \quad (2)$$

and rate of change of surface coverage:

$$\frac{\partial \theta(r,t)}{\partial t} = \left[ \frac{1}{4q} \bar{v}_A \cdot c \cdot n_A(r,t) \cdot [1 - \theta(r,t)] - P_d \cdot \theta(r,t) \right]. \quad (3)$$

Here,  $n_A$  ( $\text{m}^{-3}$ ) is volumetric reactant A number density (related to the partial pressure of the reactant  $p_A$  through the ideal gas equation),  $D_{\text{eff}}$  ( $\text{m}^2 \text{s}^{-1}$ ) is the effective diffusion coefficient,  $\theta$  (—) is surface coverage,  $\bar{s}$  (—) is the ratio of specific surface area ( $S$ ) ( $\text{m}^2 \text{g}^{-1}$ ), and pore volume ( $V_{\text{pore}}$ ) ( $\text{m}^3 \text{g}^{-1}$ ),  $\bar{v}_A$  ( $\text{m s}^{-1}$ ) is the mean thermal velocity,  $q$  ( $\text{m}^{-2}$ ) is the adsorption capacity,  $c$  (—) is the sticking coefficient, and  $P_d$  ( $\text{s}^{-1}$ ) is the desorption probability.

The effective diffusion coefficient  $D_{\text{eff}}$  in eqn (2) is calculated as<sup>56,67</sup>

$$D_{\text{eff}} = \frac{\varepsilon}{\tau} \cdot \left( \frac{1}{\frac{1}{D_A} + \frac{1}{D_{\text{Kn}}}} \right). \quad (4)$$

Here,  $D_A$  ( $\text{m}^2 \text{s}^{-1}$ ) is the molecular diffusion coefficient, which describes gas phase collisions (molecule–molecule interactions), and the  $D_{\text{Kn}}$  ( $\text{m}^2 \text{s}^{-1}$ ) is the Knudsen diffusion coefficient which dominates at low pressures and describes molecule–wall interactions. Porosity,  $\varepsilon$  (unitless) of the spheres is calculated using the relation:<sup>68</sup>

$$\varepsilon = \frac{V_{\text{pore}}}{V_{\text{pore}} + \frac{1}{\rho_s}}. \quad (5)$$

In eqn (5),  $V_{\text{pore}}$  ( $\text{cm}^3 \text{g}^{-1}$ ) is the pore volume, and  $\rho_s$  ( $\text{g cm}^{-3}$ ) is the skeletal density of the support material  $\gamma$ -alumina,  $3.6 \text{ g cm}^{-3}$ .<sup>69</sup> Tortuosity  $\tau$  (unitless) is calculated from the Beekman relationship for heterogeneous catalysts as follows:<sup>70,71</sup>

$$\tau^2 = \frac{\varepsilon}{1 - (1 - \varepsilon)^{1/3}}. \quad (6)$$

The weight percentage of the metal for a partly coated particle can be calculated by

$$w_M = \frac{q \times M_M \times S \times m_S}{N_0 \times m_t} \phi_{\text{coat}}, \quad (7)$$

where  $M_M$  ( $\text{g mol}^{-1}$ ) is the molar mass of the metal,  $S$  ( $\text{m}^2 \text{g}^{-1}$ ) is the specific surface area of the support,  $m_S$  ( $\text{g}$ ) is the mass of the support,  $N_0$  is Avogadro's constant,  $m_t$  ( $\text{g}$ ) is the total particle mass, and  $\phi_{\text{coat}}$  (—) is the coated volume fraction of the porous sphere. The  $\phi_{\text{coat}}$  is obtained from integration of the simulated saturation profile  $\theta(t_{\text{final}}, r)$  as a function of  $1 - (r/R)^3$ . For a fully coated porous sphere,  $\phi_{\text{coat}}$  is one. In the case of a step-like saturation profile with a penetration depth  $d$ , the coated volume fraction is equivalent to<sup>6,72</sup>

$$\phi_{\text{coat}} = \frac{V_d}{V_R} = \frac{(R^3 - (R-d)^3)}{R^3}, \quad (8)$$

where  $V_d$  is the coated volume, and  $V_R$  is the total internal volume of the sphere. A simplified figure showing the coated volume fraction is in the SI (Fig. S1).

## 3 Results

### 3.1 Support characterization

Support surface characteristics were studied by nitrogen physisorption. The average specific surface area, pore volume, and pore diameter values for the spheres of different diameters and the resulting aspect ratios are in Table 3. All alumina supports were mesoporous with an average pore diameter from 9.9 to 11.7 nm and a narrow pore size distribution (Figs. S3 and S4 in the SI).

### 3.2 Quantification of metal weight loading: ICP-OES

After Pt ALD using reactants MeCpPtMe<sub>3</sub> and synthetic air, the average metal weight loading on spherical alumina was determined by ICP-OES. Results for weight loadings on spheres of different diameters are presented in Fig. 1a and platinum loading in terms of the average areal number density, *i.e.*, metal atoms per support surface area, is in Fig. 1b. For spheres of all sizes, the average platinum weight loading increased with exposure time, though a slower increase was seen for the longest exposure time (1440 s). Up to 4.05 Pt wt% metal loading was observed, for sphere with a diameter of 1.8 mm (surface area =  $202 \text{ m}^2 \text{g}^{-1}$ ) at the longest exposure time (1440 s). As seen in Fig. 1b, the maximum

**Table 3** Nitrogen physisorption results: BET surface area, total pore volume, median pore radius. Calculated aspect ratio,<sup>a</sup> porosity,<sup>b</sup> and tortuosity<sup>c</sup> values are also included

| Sphere diameter (mm) | BET surface area, $S$ ( $\text{m}^2 \text{g}^{-1}$ ) | Pore volume, $V_{\text{pore}}$ ( $\text{cm}^3 \text{g}^{-1}$ ) | Average pore diameter, $d_{\text{pore}}$ (nm) | Aspect ratio <sup>a</sup> (—) | Porosity <sup>b</sup> $\varepsilon$ (—) | Tortuosity <sup>c</sup> $\tau$ (—) |
|----------------------|--|--|---|-------------------------------|---|------------------------------------|
| 1.0                  | 158  | 0.49   | 11.7  | 42 700 : 1                    | 0.64                                    | 1.49                               |
| 1.8                  | 202  | 0.55   | 10.3  | 87 300 : 1                    | 0.67                                    | 1.47                               |
| 2.5                  | 206  | 0.54   | 9.9   | 126 000 : 1                   | 0.66                                    | 1.48                               |

<sup>a</sup> Aspect ratio is calculated as the ratio of particle radius  $R$  to average pore diameter  $d_{\text{pore}}$ . <sup>b</sup> Porosity  $\varepsilon$  (—) is calculated using pore volume  $V_{\text{pore}}$  ( $\text{cm}^3 \text{g}^{-1}$ ) and the skeletal density of  $\gamma$ -alumina,  $\rho_s$  ( $3.6 \text{ g cm}^{-3}$ )<sup>69</sup> described in eqn (5). <sup>c</sup> Tortuosity  $\tau$  is calculated from the porosity using eqn (6).



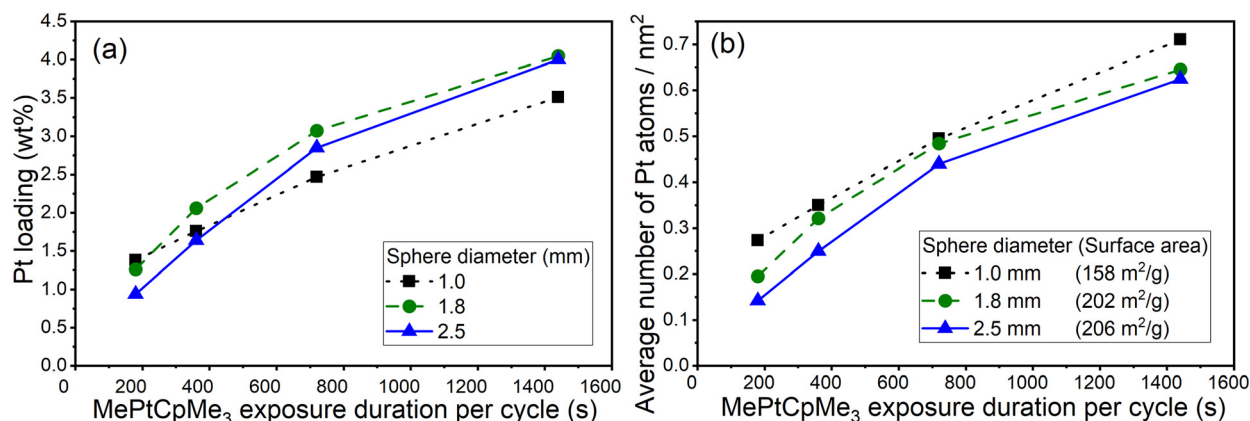


**Fig. 1** (a) Platinum loading (wt%) and (b) average platinum areal number density (atoms per nm<sup>2</sup>) as a function of the MeCpPtMe<sub>3</sub> exposure time (exposure time per cycle), based on ICP-OES and surface area of the support as in Table 3. Five ALD cycles were done at a reaction temperature of 110 °C, in a fluidized bed at atmospheric pressure. Numerical values corresponding to this figure are in Table S1 of the SI.

average areal number density after five cycles of about 0.71 Pt atoms per nm<sup>2</sup> was observed for the sphere size 1.0 mm with the highest exposure time (1440 s), with all sphere sizes showing a close value.

### 3.3 CO pulse chemisorption

Results from CO pulse chemisorption are presented in Table 4. As the ALD exposure time of the MeCpPtMe<sub>3</sub> reactant increased from 180 s to 1440 s, the cumulative quantity of CO chemisorbed on the surface initially increased and then settled. The CO adsorption capacity of the samples varied from 65 μmol g<sup>-1</sup> for the shortest exposure to 118 μmol g<sup>-1</sup> for the longest exposure. For the shortest exposure time, the number of CO molecules chemisorbed exceeds the number of platinum atoms on the surface (by ICP-OES), likely indicating an adsorption mode where one platinum atom can bind to more than one CO molecule. The dispersion calculation assumes the bonding of one CO per platinum atom (SI, Section S1.3). While for the shortest exposure time, the dispersion cannot be calculated with this assumption (it is very high, presumably ~100%), for the other exposure times, the calculated dispersion varies from 84% to 41%, and dispersion decreases with exposure time. The particle size calculated assuming hemispherical particles at the same time increases from 1.3 to 2.8 nm.

### 3.4 Surface chemical composition analysis: LEIS

LEIS reveals the presence of Pt, Al and O on the surface (example spectra in the SI, Fig. S5). Fig. 2 shows distribution maps of PtO<sub>2</sub> by LEIS and Fig. 3 gives the quantified results for the PtO<sub>2</sub> signal through the particle. Overall, the Pt penetration increased with increasing exposure time. An egg-shell coating is seen in samples with lower exposure times of 180, 360 and 720 s. For the sample with the longest exposure time of 1440 s, the coating appeared to be macroscopically uniform throughout the sample. The corresponding surface fraction of PtO<sub>2</sub> was approximately 5%. Considering that an average monolayer of PtO<sub>2</sub> has about 9.9 Pt atoms per nm<sup>2</sup> (calculated from the bulk density  $\rho = 11.8 \text{ g cm}^{-3}$ , and molar mass = 227.08 g mol<sup>-1</sup> of PtO<sub>2</sub>), the LEIS results correspond to a surface areal number density of about 0.5 Pt atoms per nm<sup>2</sup>.

### 3.5 Diffusion–reaction simulations

Diffusion–reaction simulations were made to support the experimental study. The modeling was made assuming ideal ALD, *i.e.*, saturating and irreversible adsorption steps, although the model would allow reversibility as well. Realistic parameters were chosen that are related to the ALD process conditions; the parameters are listed in the caption of Fig. 4. To have a resemblance between simulations and experiments, the partial pressure of the platinum reactant

**Table 4** Characterization results from CO pulse chemisorption (TCD measurements) done on Pt-coated alumina spheres of diameter 2.5 mm<sup>a</sup>

| MeCpPtMe <sub>3</sub> exposure time (s) | Cumulative CO quantity (cm <sup>3</sup> (STP)) | Cumulative CO quantity (μmol g <sup>-1</sup> ) | Cumulative quantity (CO molecules per nm <sup>2</sup> ) | ICP-OES weight loading (%) for 2.5 mm sphere | Average areal number density (Pt atoms per nm <sup>2</sup> ) | Metal dispersion | Crystallite size (hemisphere) (nm) |
|---|--|--|---|--|--|------------------|------------------------------------|
| 180                                     | 1.46   | 65.2   | 0.19  | 0.94   | 0.14   | — <sup>b</sup>   | — <sup>b</sup>                     |
| 360                                     | 1.59   | 70.7   | 0.21  | 1.64   | 0.25   | 84.1%            | 1.3                                |
| 720                                     | 2.67   | 119.1  | 0.35  | 2.85   | 0.44   | 81.5%            | 1.4                                |
| 1440                                    | 2.65   | 118.4  | 0.35  | 4.00   | 0.62   | 57.7%            | 2.0                                |

<sup>a</sup> Mass spectrometer results are in Table S3 of the SI. <sup>b</sup> The cumulative quantity of CO chemisorbed exceeded the number of Pt atoms, and dispersion can be assumed to be approximately 100%. The stoichiometry of adsorption may differ from the stoichiometry value of one, assumed in the dispersion and crystallite size calculations.



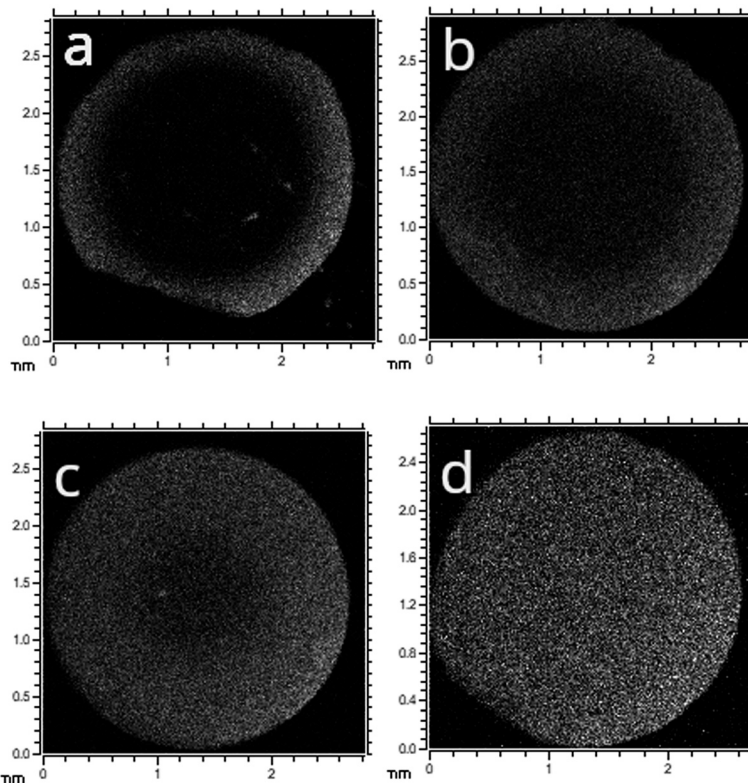


**Fig. 2** Low-energy ion scattering (LEIS) qualitative maps showing platinum surface across cross-sections of 2.5 mm (diameter) ALD coated Pt/Al<sub>2</sub>O<sub>3</sub> spheres. Brighter areas indicate higher surface coverage of platinum. The platinum reactant exposure time per cycle was (a) 180 s, (b) 360 s, (c) 720 s, and (d) 1440 s.

and the sticking coefficient were varied (the average areal number density of platinum was assumed as 0.12 nm<sup>-2</sup>). To have results similar to LEIS (and X-ray photoelectron spectroscopy, see SI section S2.6) that show through-penetration (uniform macroscopic distribution) for the

exposure times of 1440 s, the sticking coefficient had to be made very small, on the order of 10<sup>-9</sup>.

## 4 Discussion

### 4.1 Comparison of Pt loading to literature values

The Pt metal loading observed in this study is consistent with values for platinum reported in the literature for ALD on particulate materials. To enable comparison with literature, the average areal number density was calculated from the reported values of Pt weight loading. In this work, the weight loading for the longest exposure time (1440 s) ranged from 3.5 wt% for the 1.0 mm sphere to 4 wt% for the 2.5 mm sphere (Fig. 1). These weight loadings translate to growth per cycle (GPC) in terms of average areal number density of 0.71 and 0.62 atoms per nm<sup>2</sup> after five cycles, or ~0.14 and 0.12 Pt atoms per nm<sup>2</sup> per cycle for the sphere sizes 1.0 and 2.5 mm, respectively (Table S1). The GPC of 0.14 and 0.12 Pt atoms per nm<sup>2</sup> corresponds to approximately 1% of an average Pt monolayer, calculated from the bulk density and mass of Pt (see eqn (16) in ref. 73,  $\rho = 21.45 \text{ g cm}^{-3}$ , areal number density of an average platinum monolayer  $c_M^{\text{ml}} \approx 16.4 \text{ atoms per nm}^2$ ).

The values of average areal number density estimated from the literature data vary over a broad range. For example, with MeCpPtMe<sub>3</sub> on mesoporous silica gel at 325 °C, the Pt loading corresponds to an average areal number density of

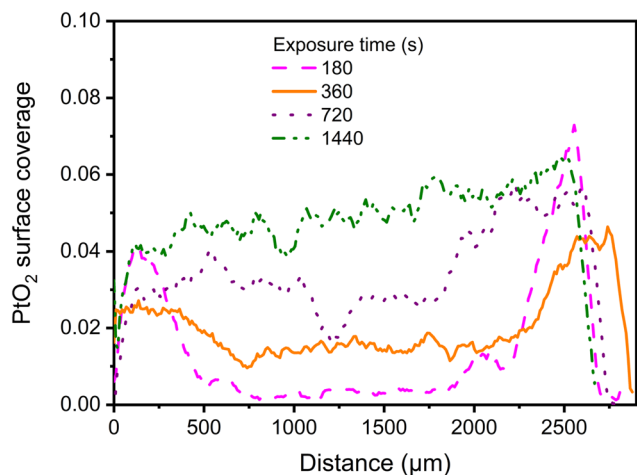


**Fig. 3** Quantified line scans of the LEIS images in Fig. 2 for ALD coated Pt/Al<sub>2</sub>O<sub>3</sub> spheres (diameter: 2.5 mm). The horizontal line scans through the center of the alumina spheres are averaged over 16 pixels in the vertical direction and are plotted with 11-point adjacent averaging.



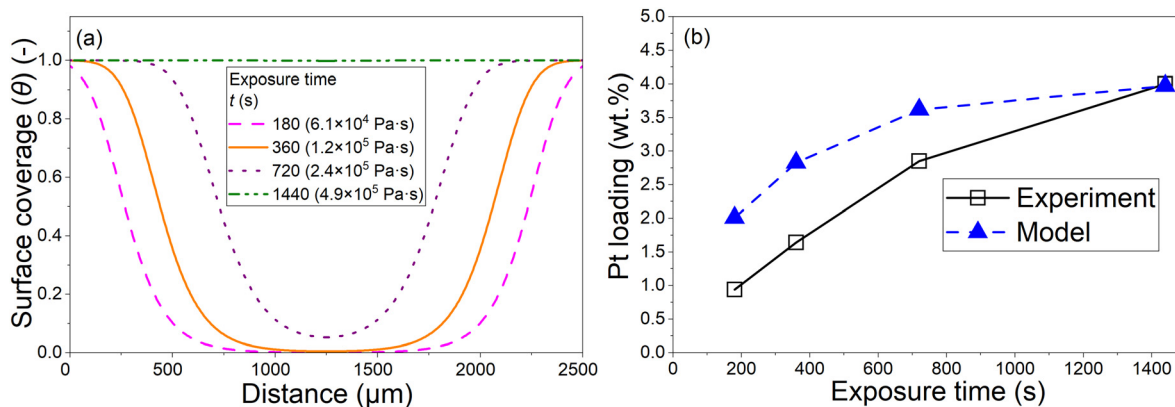


**Fig. 4** (a) Simulated surface coverage profiles, along the radial direction from the outer surface towards the center and back, along the radius of a 2.5 mm alumina sphere. (b) Comparison of the average Pt weight loading from the model to the experiments (ICP-OES results in Fig. 1). The sticking coefficient used for the simulation was  $10^{-9}$ . Corresponding pressure profiles are shown in the SI (Fig. S8). Other parameters were: reactant was MeCpPtMe<sub>3</sub>; particle diameter = 2.5 mm ( $R = 0.00125$  m);  $\varepsilon = 0.66$ ;  $\tau = 1.5$ ;  $d_{\text{pore}} = 9.9$  nm;  $S = 206$  m<sup>2</sup> g<sup>-1</sup>;  $V_{\text{pore}} = 5.4 \times 10^{-7}$  m<sup>3</sup> g<sup>-1</sup>;  $\rho_s = 3600$  kg m<sup>-3</sup>;  $q = 0.12$  nm<sup>-2</sup>;  $P_d = 0$  s<sup>-1</sup>;  $T = 383$  K;  $p_{A0} = 340$  Pa;  $p_l = 99660$  Pa; the molar mass of reactant  $M_A = 0.319$  kg mol<sup>-1</sup>; the molar mass of inert  $M_I = 0.028$  kg mol<sup>-1</sup>;  $d_A = 8.13 \times 10^{-10}$  m;  $d_I = 3.74 \times 10^{-10}$  m;  $M_M = 0.195$  kg mol<sup>-1</sup>. The calculated Kn number was  $\sim 1.4$  (transition region) and the Thiele modulus was  $\sim 12$  (diffusion-limited process), see SI section S1.2.

0.03 atoms per nm<sup>2</sup> per cycle (over three cycles).<sup>59</sup> For another study with MeCpPtMe<sub>3</sub> on graphene nanoplatelets at 100 °C the average areal number density corresponds to 0.13 atoms per nm<sup>2</sup> per cycle (over 10 cycles)<sup>74</sup> and on carbon black at 300 °C corresponds to 0.16 atoms per nm<sup>2</sup> per cycle (over 15 cycles).<sup>75</sup> On other types of carbon supports, even higher average areal number density values were also observed. For example in the case of MeCpPtMe<sub>3</sub> on multi-walled carbon nanotubes<sup>30,76</sup> at 300 °C (one cycle), average areal number density corresponds to 0.49 atoms per nm<sup>2</sup> and on carbon (Vulcan XC72R) at 300 °C for fuel cells,<sup>77</sup> average areal number density corresponds to 2.2 atoms per nm<sup>2</sup> per cycle (over five cycles). Overall, the literature range for Pt average areal number density is broad, from 0.03 (ref. 59) up to 2.2 (ref. 77) atoms per nm<sup>2</sup> per cycle. The average areal number density results of this work, values between 0.14 to 0.12 Pt atoms per nm<sup>2</sup> per cycle fall well within the range observed in previous literature.

#### 4.2 Choice of a low sticking coefficient for simulations

For simulations, a resemblance with experimental saturation profile data can be achieved only with the selection of a low sticking coefficient. In this case, we used a sticking coefficient of  $10^{-9}$  which is lower than most sticking coefficient values reported previously for metal ALD.<sup>3,78</sup> With higher sticking coefficients of the order of  $10^{-6}$ , and  $10^{-3}$ , a step-like saturation profile was seen, with an abrupt adsorption front (SI Fig. S9). The low sticking coefficient may be linked to the nucleation delay reported for MePtCpMe<sub>3</sub>/O<sub>2</sub> in earlier studies.<sup>79–81</sup> Also, the ALD temperature in our study, 110 °C, which was lower than that reported in most of the literature for Pt ALD on particulate materials, which typically used  $\sim 300$  °C<sup>30,75–77,82,83</sup> and the low temperature may be linked to the low sticking coefficient. As shown

previously,<sup>74,84</sup> using a low deposition temperature is possible because operating at atmospheric pressure allows a higher partial pressure of O<sub>2</sub>, enabling the process to proceed at a lower temperature. This temperature was chosen for the ALD process because lower process temperatures typically lead to a narrower particle size distribution and more stable Pt catalysts.<sup>74</sup>

#### 4.3 Pt particle size

With increasing ALD exposure time of MeCpPtMe<sub>3</sub>, there was an increase in Pt crystallite size and a decrease in dispersion seen from the CO chemisorption results (Table 4). The increase in particle size may be related to a slow increase of Pt uptake with longer exposure time (Table S2 in the SI).<sup>79,85</sup> This increasing Pt particle size might also be explained by Ostwald particle ripening phenomena<sup>86</sup> and/or island aggregation.<sup>87</sup> Coalescence-driven growth of Pt has been reported elsewhere, where particle size evolution was largely governed by surface migration and diffusion-driven coalescence rather than precursor adsorption alone.<sup>79,88</sup>

#### 4.4 Comparison to state of the art mesoporous particle coating by ALD

The results of this work seem to indicate that the platinum reactant does not thermally decompose at the used ALD reaction temperature (110 °C). It was previously shown through Monte Carlo simulations<sup>3</sup> that for processes that in addition to ideal ALD include a continuous CVD-type decomposition component, thermal decomposition would be expected to manifest itself through a higher platinum content in the outer areas of the particles. The absence of such a concentration gradient points to the absence of thermal decomposition.



In this work, a uniform Pt distribution was obtained for porous spheres with an AR of 126 000:1 (AR, taken as the ratio of the particle radius to the pore diameter). Previously, to the authors' knowledge on porous spheres (see Table 1), the highest previously reported AR was 43 103:1 (ref. 48) for which a uniform distribution by noble metal ALD (Ru(EtCp)<sub>2</sub>/O<sub>2</sub> process) was seen. For Pt, uniform coating on mesoporous silica gel particles (size: 30–75 μm) was shown up to an AR of 6250:1 using a MeCpPtMe<sub>3</sub>/O<sub>2</sub> process in a fluidized bed reactor operated at vacuum conditions.<sup>59</sup> In the case of a Pd(hfac)<sub>2</sub>/formalin process on porous alumina spheres with extremely high aspect ratios (~125 000:1), only a thin egg-shell type coating was demonstrated.<sup>46</sup>

Other studies have also demonstrated uniform distribution in porous high aspect ratio materials with different shapes than spheres. On silica aerogel monolith slabs, the penetration depth increased with increasing exposure time and uniform coating was seen for AR 60 000:1.<sup>89,90</sup> On mesoporous alumina (size: 125–300 μm) with AR up to 12 500:1, a TiO<sub>2</sub> overcoat extending through the alumina support was observed (Ti[OCH(CH<sub>3</sub>)<sub>2</sub>]<sub>4</sub>/H<sub>2</sub>O process) with some additional titanium around the edges of the particles,<sup>91</sup> which may suggest the presence of some CVD type decomposition in addition to ALD.<sup>3</sup>

In conclusion, while uniform ALD coatings on mesoporous supports have been previously reported before under specific ALD process conditions, the present work extends such uniformity to significantly higher aspect ratios, *ca.* 125 000:1.

## 5 Conclusion

In this work, ALD of Pt on mesoporous alumina spheres was shown using (methylcyclopentadienyl)trimethyl platinum [MeCpPtMe<sub>3</sub>] and synthetic air at 110 °C in a fluidized bed reactor operated at atmospheric pressure. Macroscopic distribution of platinum, analyzed by LEIS, varied from egg-shell to uniform, depending on the exposure time. Uniform distribution could be obtained even on spheres of 2.5 mm diameter, with an aspect ratio of *ca.* 125 000:1 (ratio of particle radius to average pore diameter). For the longest exposure time (2880 s) and five ALD cycles, a Pt weight loading on the order of 3.5 to 4 wt% was obtained, giving an average GPC, expressed as average areal number density, of 0.14 to 0.12 Pt atoms per nm<sup>2</sup>.

A diffusion–reaction model for porous spheres<sup>56</sup> was used to simulate Pt distribution. In order to make the modeling results resemble the experimental results, a very low sticking coefficient (on the order of 10<sup>−9</sup>) had to be assumed. This is likely in line with the strong nucleation delay observed for this process. The diffusion–reaction simulations, based on the ideal ALD assumption (*i.e.*, saturating, irreversible reactions) were able to reproduce the main features of the process.

## Author contributions

Christine Gonsalves: data curation, formal analysis, investigation, methodology, validation, visualization, writing – original draft, writing – review and editing. Jänis Järvillehto: conceptualization, data curation, formal analysis, investigation, methodology, validation, visualization, writing – original draft, writing – review and editing. Saeed Saedy: conceptualization, data curation, investigation, methodology, validation, writing – review and editing. Jorge A. Velasco: investigation, methodology, software, supervision, writing – original draft, writing – review and editing. Philipp Brüner: data curation, investigation, visualization, writing – original draft, writing – review and editing. Thomas Grehl: data curation, supervision. Niko Heikkinen: investigation, software, validation. Juha Lehtonen: software, supervision. Ruud van Ommen: conceptualization, methodology, resources, supervision, writing – review and editing. Riikka Puurunen: conceptualization, funding acquisition, methodology, project administration, resources, supervision, writing – review and editing.

## Conflicts of interest

There are no conflicts of interest to declare.

## List of symbols

|               |   |
|---------------|---|
| $c$           | Sticking coefficient (—)  |
| $c_M$         | Areal number density (nm <sup>−2</sup> )  |
| $D_A$         | Molecular diffusion coefficient (m <sup>2</sup> s <sup>−1</sup> )   |
| $D_{eff}$     | Effective diffusion coefficient (m <sup>2</sup> s <sup>−1</sup> )   |
| $D_{Kn}$      | Knudsen diffusion coefficient (m <sup>2</sup> s <sup>−1</sup> )   |
| $d_A$         | Hard-sphere diameter of molecule A (m)  |
| $d_I$         | Hard-sphere diameter of the inert gas molecule (m)  |
| $d_{pore}$    | Pore diameter of the support (m)  |
| $\epsilon$    | Porosity (—)  |
| $\phi_{coat}$ | Coated volume fraction ( $V_d/V_R$ ) of the porous sphere (—)   |
| Kn            | Knudsen number  |
| $m_s$         | Mass of the support (g)   |
| $m_t$         | Total mass of the sample (g)  |
| $M_M$         | Molar mass of the metal (g mol <sup>−1</sup> )  |
| $M_A$         | Molar mass of reactant A (kg mol <sup>−1</sup> )  |
| $M_I$         | Molar mass of inert gas I (kg mol <sup>−1</sup> )   |
| $n$           | Stoichiometric factor (number of CO molecules adsorbed per surface metal atom) (—)  |
| $n_A$         | Volumetric reactant A number density (m <sup>−3</sup> )   |
| $N_0$         | Avogadro's constant (mol <sup>−1</sup> )  |
| $P_d$         | Desorption probability (s <sup>−1</sup> )   |
| $q$           | Adsorption capacity of metal M atoms in the ALD growth of film of the M <sub>y</sub> Z <sub>x</sub> material (nm <sup>−2</sup> ) ( <i>i.e.</i> , GPC expressed as areal number density) |
| $\rho_s$      | Skeletal density of the support, here $\gamma$ -alumina 3.6 g cm <sup>−3</sup> (ref. 69)  |
| $S$           | Specific surface area of the support (m <sup>2</sup> g <sup>−1</sup> )  |
| $\bar{s}$     | Ratio of surface area ( $S$ ) and pore volume (—)( $V_{pore}$ )   |



|                   |   |
|-------------------|---|
| $\tau$            | Tortuosity (—)  |
| $\theta$          | Surface coverage (—)  |
| $t$               | Time (s)  |
| $T$               | Temperature (K)   |
| $\bar{v}_A$       | Thermal velocity of molecule A ( $\text{m s}^{-1}$ )        |
| $V_d$             | Coated volume of the sphere ( $\text{cm}^3 \text{g}^{-1}$ ) |
| $V_{\text{pore}}$ | Pore volume ( $\text{cm}^3 \text{g}^{-1}$ )                 |
| $V_R$             | Total volume of a sphere ( $\text{cm}^3 \text{g}^{-1}$ )    |
| $w_M$             | Weight fraction of the metal (%)                            |

## Data availability

The simulation code used for the diffusion–reaction model of porous spheres will be made publicly available as open research software on GitHub ([https://github.com/Aalto-Puurunen/ALD\\_porous-sphere\\_JV](https://github.com/Aalto-Puurunen/ALD_porous-sphere_JV)). Data will be made available upon reasonable request.

Supplementary information (SI) is available. See DOI: <https://doi.org/10.1039/d5lf00395d>.

## Acknowledgements

The authors thank Dirk Niemeyer (SASOL Ltd.) for providing the alumina supports. C. G. thanks Reetta Karinen for fruitful discussions and feedback. This work was financially supported by the Research Council of Finland (former Academy of Finland) ALDI consortium, decision no. 331082; by the Vilho, Yrjö and Kalle Väisälä Foundation of the Finnish Academy of Science and Letters; by the Business Finland project Forest CUMP (Dnro 2158/31/2022); and by the Business Finland project e-Fuel (Dnro 43287/31/2020). C. G. thanks the Walter Ahlström foundation for an encouragement grant. Computational resources were provided by the Aalto Science-IT services, and CSC – IT Center for Science, Finland.

## References

- J. R. van Ommen, A. Goulas and R. L. Puurunen, in *Kirk-Othmer Encyclopedia of Chemical Technology*, John Wiley & Sons, Ltd, 2021, pp. 1–42.
- R. L. Puurunen, Surface chemistry of atomic layer deposition: A case study for the trimethylaluminum/water process, *J. Appl. Phys.*, 2005, **97**, 121301.
- V. Cremers, R. L. Puurunen and J. Dendooven, Conformality in atomic layer deposition: Current status overview of analysis and modelling, *Appl. Phys. Rev.*, 2019, **6**, 021302.
- V. Miikkulainen, M. Leskelä, M. Ritala and R. L. Puurunen, Crystallinity of inorganic films grown by atomic layer deposition: Overview and general trends, *J. Appl. Phys.*, 2013, **113**, 021301.
- G. Popov, M. Mattinen, A. Vihervaara and M. Leskelä, Recent trends in thermal atomic layer deposition chemistry, *J. Vac. Sci. Technol.*, A, 2025, **43**, 030801.
- C. Detavernier, J. Dendooven, S. P. Sree, K. F. Ludwig and J. A. Martens, Tailoring nanoporous materials by atomic layer deposition, *Chem. Soc. Rev.*, 2011, **40**, 5242–5253.
- J. R. van Ommen and A. Goulas, Atomic layer deposition on particulate materials, *Mater. Today Chem.*, 2019, **14**, 100183.
- J. Yim, E. Haimi, M. Mäntymäki, V. Kärkäs, R. Bes, A. A. Gutierrez, K. Meinander, P. Brüner, T. Grehl, L. Gell, T. Viinikainen, K. Honkala, S. Huotari, R. Karinen, M. Putkonen and R. L. Puurunen, Atomic Layer Deposition of Zinc Oxide on Mesoporous Zirconia Using Zinc(II) Acetylacetonate and Air, *Chem. Mater.*, 2023, **35**, 7915–7930.
- B. J. O'Neill, D. H. K. Jackson, J. Lee, C. Canlas, P. C. Stair, C. L. Marshall, J. W. Elam, T. F. Kuech, J. A. Dumesic and G. W. Huber, Catalyst Design with Atomic Layer Deposition, *ACS Catal.*, 2015, **5**, 1804–1825.
- A. Arandia, J. A. Velasco, A. Sajid, J. Yim, H. Shamshad, H. Jiang, A. Chahal, A. K. Singh, C. Gonsalves, R. Karinen and R. L. Puurunen, Atomic layer deposited zinc promoted copper catalysts for carbon dioxide hydrogenation to methanol: Influence of support, *Catal. Today*, 2025, **454**, 115283.
- Y. Koshtyal, D. Olkhovskii, A. Romyantsev and M. Maximov, Applications and Advantages of Atomic Layer Deposition for Lithium-Ion Batteries Cathodes: Review, *Batteries*, 2022, **8**, 184.
- R. Saleh, A. Memarzadeh, D. Hurdoganoglu, S. Sahmani, T.-C. Jen and B. Safaei, A comprehensive review on atomic layer deposition on key components in fuel cells, *Fuel*, 2025, **395**, 135172.
- R. Verstraete, G. Rampelberg, H. Rijckaert, I. Van Driessche, E. Coetsee, M.-M. Duvenhage, P. F. Smet, C. Detavernier, H. Swart and D. Poelman, Stabilizing fluoride phosphors: surface modification by atomic layer deposition, *Chem. Mater.*, 2019, **31**, 7192–7202.
- Z. Zhou, N. Zhou, X. Lu, M. Ten Kate, D. Valdesueiro, J. R. Van Ommen and H. B. Hintzen, Performance improvement by alumina coatings on  $\text{Y}_3\text{Al}_5\text{O}_{12}$ :  $\text{Ce}^{3+}$  phosphor powder deposited using atomic layer deposition in a fluidized bed reactor, *RSC Adv.*, 2016, **6**, 76454–76462.
- F. Zhang, K. Wu, D. La Zara, F. Sun, M. J. Quayle, G. Petersson, S. Folestad, J. W. Chew and J. R. Van Ommen, Tailoring the flow properties of inhaled micronized drug powders by atomic and molecular layer deposition, *Chem. Eng. J.*, 2023, **462**, 142131.
- P. M. Piechulla, M. Chen, A. Goulas, R. L. Puurunen and J. R. van Ommen, Atomic layer deposition on particulate materials from 1988 through 2023: A quantitative review of technologies, materials, and applications, *Chem. Mater.*, 2026, **38**(1), 20–86.
- A. Goulas and J. R. van Ommen, Scalable production of nanostructured particles using atomic layer deposition, *Kona Powder Part. J.*, 2014, **31**, 234–246.
- X. Ren, Q. Lv, L. Liu, B. Liu, Y. Wang, A. Liu and G. Wu, Current progress of Pt and Pt-based electrocatalysts used for fuel cells, *Sustainable Energy Fuels*, 2020, **4**, 15–30.
- R. J. Spiegel, Platinum and fuel cells, *Transp. Res. D Trans. Environ.*, 2004, **9**, 357–371.
- O. T. Holton and J. W. Stevenson, The role of platinum in proton exchange membrane fuel cells, *Platinum Met. Rev.*, 2013, **57**, 259–271.



- 21 P. Rylander, *Catalytic hydrogenation over platinum metals*, Elsevier, 2012.
- 22 S. Yang, J. Kim, Y. J. Tak, A. Soon and H. Lee, Single-Atom Catalyst of Platinum Supported on Titanium Nitride for Selective Electrochemical Reactions, *Angew. Chem., Int. Ed.*, 2016, **55**, 2058–2062.
- 23 G. Pardon, H. K. Gatty, G. Stemme, W. v. d. Wijngaart and N. Roxhed, Pt-Al<sub>2</sub>O<sub>3</sub> dual layer atomic layer deposition coating in high aspect ratio nanopores, *Nanotechnology*, 2012, **24**, 015602.
- 24 A. Vaish, S. Krueger, M. Dimitriou, C. Majkrzak, D. J. Vanderah, L. Chen and K. Gawrisch, Enhancing the platinum atomic layer deposition infiltration depth inside anodic alumina nanoporous membrane, *J. Vac. Sci. Technol., A*, 2014, **33**, 01A148.
- 25 D. Gu, H. Baumgart, K. Tapily, P. Shrestha, G. Namkoong, X. Ao and F. Müller, Precise control of highly ordered arrays of nested semiconductor/metal nanotubes, *Nano Res.*, 2011, **4**, 164–170.
- 26 F. Bíró, C. Dücső, G. Z. Radnóczy, Z. Baji, M. Takács and I. Bársony, ALD nano-catalyst for micro-calorimetric detection of hydrocarbons, *Sens. Actuators, B*, 2017, **247**, 617–625.
- 27 S. Galbiati, A. Morin and N. Pauc, Supportless Platinum Nanotubes Array by Atomic Layer Deposition as PEM Fuel Cell Electrode, *Electrochim. Acta*, 2014, **125**, 107–116.
- 28 J. Zhang, W. Yu, D. Feng, H. Xu and Y. Qin, Porous titania nanotube confined ultrafine platinum catalysts synthesized by atomic layer deposition with enhanced hydrolytic dehydrogenation performance, *Appl. Catal., B*, 2022, **312**, 121405.
- 29 J. Zhang, Z. Yu, Z. Gao, H. Ge, S. Zhao, C. Chen, S. Chen, X. Tong, M. Wang, Z. Zheng and Y. Qin, Porous TiO<sub>2</sub> nanotubes with spatially separated platinum and CoO<sub>x</sub> cocatalysts produced by atomic layer deposition for photocatalytic hydrogen production, *Angew. Chem., Int. Ed.*, 2017, **56**, 816–820.
- 30 X. Liang and C. Jiang, Atomic layer deposited highly dispersed platinum nanoparticles supported on non-functionalized multiwalled carbon nanotubes for the hydrogenation of xylose to xylitol, *J. Nanopart. Res.*, 2013, **15**, 1890.
- 31 I. J. M. Erkens, M. A. Verheijen, H. C. M. Knoops, W. Keuning, F. Roozeboom and W. M. M. Kessels, Plasma-assisted atomic layer deposition of conformal Pt films in high aspect ratio trenches, *J. Chem. Phys.*, 2016, **146**, 052818.
- 32 Y. Zhu, K. A. Dunn and A. E. Kaloyeros, Properties of ultrathin platinum deposited by atomic layer deposition for nanoscale copper-metallization schemes, *J. Mater. Res.*, 2007, **22**, 1292–1298.
- 33 D. J. Hagen, J. Yoon, H. Zhang, B. Kalkofen, M. Silinskas, F. Börrnert, H. Han and S. S. P. Parkin, Atomic Layer Deposition of the Conductive Delafossite PtCoO<sub>2</sub>, *Adv. Mater. Interfaces*, 2022, **9**, 2200013.
- 34 S.-M. Han, D. K. Nandi, Y.-H. Joo, T. Shigetomi, K. Suzuki, S. Nabeya, R. Harada and S.-H. Kim, Atomic layer deposition of high-quality Pt thin film as an alternative interconnect replacing Cu, *J. Vac. Sci. Technol., A*, 2020, **38**, 032404.
- 35 J. Hämäläinen, E. Puukilainen, T. Sajavaara, M. Ritala and M. Leskelä, Low temperature atomic layer deposition of noble metals using ozone and molecular hydrogen as reactants, *Thin Solid Films*, 2013, **531**, 243–250.
- 36 J. Lee, J. Yoon, H. G. Kim, S. Kang, W.-S. Oh, H. Algadi, S. Al-Sayari, B. Shong, S.-H. Kim, H. Kim, T. Lee and H.-B.-R. Lee, Highly conductive and flexible fiber for textile electronics obtained by extremely low-temperature atomic layer deposition of Pt, *NPG Asia Mater.*, 2016, **8**, e331.
- 37 W.-J. Lee, Z. Wan, C.-M. Kim, I.-K. Oh, R. Harada, K. Suzuki, E.-A. Choi and S.-H. Kwon, Atomic Layer Deposition of Pt Thin Films Using Dimethyl (N,N-Dimethyl-3-Butene-1-Amine-N) Platinum and O<sub>2</sub> Reactant, *Chem. Mater.*, 2019, **31**, 5056–5064.
- 38 Y. Son, S. B. Kim, D. Mohapatra, T. Cheon and S.-H. Kim, Advanced Atomic Layer Modulation Based Highly Homogeneous PtRu Precious Metals Alloy Thin Films, *Adv. Sci.*, 2025, **12**(29), e03561.
- 39 T. Aaltonen, A. Rahtu, M. Ritala and M. Leskelä, Reaction mechanism studies on atomic layer deposition of ruthenium and platinum, *Electrochem. Solid-State Lett.*, 2003, **6**, C130–C133.
- 40 H. Van Bui, F. Grillo, D. M. Nguyen, M. D. Dang, A. A. Aarnink, R. A. Wolters, J. R. van Ommen and A. Y. Kovalgin, Highly Reactive Atomic Hydrogen as an Alternative Reactant for Atomic Layer Deposition of Platinum Using MeCpPtMe<sub>3</sub>, *J. Phys. Chem. C*, 2025, **129**(30), 13822–13829.
- 41 S. Kwon and B. Shong, Chemical mechanism for nucleation enhancement in atomic layer deposition of Pt by surface functionalization, *J. Vac. Sci. Technol., A*, 2025, **43**, 012401.
- 42 L.-A. T. Le, H. T. Ta, H. V. Bui and N. L. Nguyen, Atomic Layer Deposition of Platinum on the Oxygen-Pretreated Graphene Surface, *J. Phys. Chem. C*, 2024, **129**, 705–714.
- 43 H.-E. Nieminen, M. Putkonen and M. Ritala, In vacuo studies on reaction mechanisms in ALD processes of ruthenium and platinum films, *Appl. Surf. Sci.*, 2024, **648**, 159015.
- 44 N. Heikkinen, J. Lehtonen, L. Keskiaväli, J. Yim, S. Shetty, Y. Ge, M. Reinikainen and M. Putkonen, Modelling atomic layer deposition overcoating formation on a porous heterogeneous catalyst, *Phys. Chem. Chem. Phys.*, 2022, **24**, 20506–20516.
- 45 S. W. Han, D. H. Kim, M.-G. Jeong, K. J. Park and Y. D. Kim, CO oxidation catalyzed by NiO supported on mesoporous Al<sub>2</sub>O<sub>3</sub> at room temperature, *Chem. Eng. J.*, 2016, **283**, 992–998.
- 46 A. C. Bueno, M. Mayer, M. Weber, M. Bechelany, M. Klotz and D. Farrusseng, Impregnation Protocols on Alumina Beads for Controlling the Preparation of Supported Metal Catalysts, *Catalysts*, 2019, **9**, 577.
- 47 J. W. Elam, J. A. Libera, T. H. Huynh, H. Feng and M. J. Pellin, Atomic Layer Deposition of Aluminum Oxide in Mesoporous Silica Gel, *J. Phys. Chem. C*, 2010, **114**, 17286–17292.



- 48 I. H. Kim, M.-G. Jeong, S. W. Han, E. J. Park, Y. K. Hwang and Y. D. Kim, CO oxidation catalyzed by RuO<sub>2</sub> nanoparticles supported on mesoporous Al<sub>2</sub>O<sub>3</sub> prepared via atomic layer deposition, *Curr. Appl. Phys.*, 2016, **16**, 1407–1412.
- 49 G. Ballai, T. Kotnik, M. Finšgar, A. Pintar, Z. Kónya, A. Sápi and S. Kovačič, Highly Porous Polymer Beads Coated with Nanometer-Thick Metal Oxide Films for Photocatalytic Oxidation of Bisphenol A, *ACS Appl. Nano Mater.*, 2023, **6**, 20089–20098.
- 50 R. G. Gordon, D. Hausmann, E. Kim and J. Shepard, A Kinetic Model for Step Coverage by Atomic Layer Deposition in Narrow Holes or Trenches, *Chem. Vap. Deposition*, 2003, **9**, 73–78.
- 51 M. Ylilammi, O. M. E. Ylivaara and R. L. Puurunen, Modeling growth kinetics of thin films made by atomic layer deposition in lateral high-aspect-ratio structures, *J. Appl. Phys.*, 2018, **123**, 205301.
- 52 J. Yim, E. Verkama, J. A. Velasco, K. Arts and R. L. Puurunen, Conformality of atomic layer deposition in microchannels: impact of process parameters on the simulated thickness profile, *Phys. Chem. Chem. Phys.*, 2022, **24**, 8645–8660.
- 53 J. Järvillehto, J. A. Velasco, J. Yim, C. Gonsalves and R. L. Puurunen, Simulation of conformality of ALD growth inside lateral channels: comparison between a diffusion-reaction model and a ballistic transport-reaction model, *Phys. Chem. Chem. Phys.*, 2023, **25**, 22952–22964.
- 54 C. Gonsalves, J. A. Velasco, J. Yim, J. Järvillehto, V. Vuorinen and R. L. Puurunen, Simulated conformality of atomic layer deposition in lateral channels: the impact of the Knudsen number on the saturation profile characteristics, *Phys. Chem. Chem. Phys.*, 2024, **26**, 28431–28448.
- 55 R. A. Adomaitis, A Ballistic Transport and Surface Reaction Model for Simulating Atomic Layer Deposition Processes in High-Aspect-Ratio Nanopores, *Chem. Vap. Deposition*, 2011, **17**, 353–365.
- 56 N. Heikkinen, J. Lehtonen and R. L. Puurunen, An atomic layer deposition diffusion-reaction model for porous media with different particle geometries, *Phys. Chem. Chem. Phys.*, 2024, **26**, 7580–7591.
- 57 N. Heikkinen, *Doctoral thesis*, Aalto University, 2025.
- 58 J. Libera, J. Elam and M. Pellin, Conformal ZnO coatings on high surface area silica gel using atomic layer deposition, *Thin Solid Films*, 2008, **516**, 6158–6166.
- 59 J. Li, X. Liang, D. M. King, Y.-B. Jiang and A. W. Weimer, Highly dispersed Pt nanoparticle catalyst prepared by atomic layer deposition, *Appl. Catal., B*, 2010, **97**, 220–226.
- 60 F. Grillo, H. Van Bui, D. La Zara, A. A. Aarnink, A. Y. Kovalgin, P. Kooyman, M. T. Kreutzer and J. R. van Ommen, From single atoms to nanoparticles: Autocatalysis and metal aggregation in atomic layer deposition of Pt on TiO<sub>2</sub> nanopowder, *Small*, 2018, **14**, 1800765.
- 61 A. Goulas and J. Ruud Van Ommen, Atomic layer deposition of platinum clusters on titania nanoparticles at atmospheric pressure, *J. Mater. Chem. A*, 2013, **1**, 4647.
- 62 D. Valdesueiro, G. M. Meesters, M. T. Kreutzer and J. R. Van Ommen, Gas-phase deposition of ultrathin aluminium oxide films on nanoparticles at ambient conditions, *Materials*, 2015, **8**, 1249–1263.
- 63 F. Grillo, M. T. Kreutzer and J. R. van Ommen, Modeling the precursor utilization in atomic layer deposition on nanostructured materials in fluidized bed reactors, *Chem. Eng. J.*, 2015, **268**, 384–398.
- 64 S. Brunauer, P. H. Emmett and E. Teller, Adsorption of gases in multimolecular layers, *J. Am. Chem. Soc.*, 1938, **60**, 309–319.
- 65 B. C. Lippens, B. G. Linsen and J. H. d. Boer, Studies on pore systems in catalysts I. The adsorption of nitrogen; apparatus and calculation, *J. Catal.*, 1964, **3**, 32–37.
- 66 J. A. Velasco and R. L. Puurunen, *Diffusion-reaction model for ALD on porous spheres* [GitHub Repository], 2025, [https://github.com/Aalto-Puurunen/ALD\\_porous-sphere\\_JV](https://github.com/Aalto-Puurunen/ALD_porous-sphere_JV).
- 67 R. Evans III, G. Watson and E. Mason, Gaseous diffusion in porous media at uniform pressure, *J. Chem. Phys.*, 1961, **35**, 2076–2083.
- 68 C. H. Bartholomew and R. J. Farrauto, *Catalyst Materials, Properties and Preparation*, John Wiley & Sons, Inc., 2nd edn, 2005, pp. 60–117.
- 69 H. Hashimoto, Y. Onodera, S. Tahara, S. Kohara, K. Yazawa, H. Segawa, M. Murakami and K. Ohara, Structure of alumina glass, *Sci. Rep.*, 2022, **12**, 516.
- 70 J. Beeckman, Mathematical description of heterogeneous materials, *Chem. Eng. Sci.*, 1990, **45**, 2603–2610.
- 71 L. Shen and Z. Chen, Critical review of the impact of tortuosity on diffusion, *Chem. Eng. Sci.*, 2007, **62**, 3748–3755.
- 72 J. Dendooven, *Atomically-Precise Methods for Synthesis of Solid Catalysts*, Royal Society of Chemistry, Cambridge, UK, 2014, vol. 22.
- 73 R. L. Puurunen, Growth per cycle in atomic layer deposition: a theoretical model, *Chem. Vap. Deposition*, 2003, **9**, 249–257.
- 74 H. Van Bui, F. Grillo, S. S. Kulkarni, R. Bevaart, N. Van Thang, B. Van Der Linden, J. A. Moulijn, M. Makkee, M. T. Kreutzer and J. R. Van Ommen, Low-temperature atomic layer deposition delivers more active and stable Pt-based catalysts, *Nanoscale*, 2017, **9**, 10802–10810.
- 75 W.-J. Lee and S.-H. Kwon, Role of Acid Treatment of the Carbon Support in the Growth of Atomic-Layer-Deposited Pt Nanoparticles for PEMFC Fabrication, *Part. Part. Syst. Charact.*, 2023, **40**, 2200158.
- 76 C. Jiang and X. Liang, Catalytic hydrogen transfer of ketones over atomic layer deposited highly-dispersed platinum nanoparticles supported on multi-walled carbon nanotubes, *Catal. Commun.*, 2014, **46**, 41–45.
- 77 A. M. Lubers, C. L. Muhich, K. M. Anderson and A. W. Weimer, Mechanistic studies for depositing highly dispersed Pt nanoparticles on carbon by use of trimethyl (methylcyclopentadienyl) platinum (IV) reactions with O<sub>2</sub> and H<sub>2</sub>, *J. Nanopart. Res.*, 2015, **17**, 179.
- 78 J. Yim, O. M. Ylivaara, M. Ylilammi, V. Korpelainen, E. Haimi, E. Verkama, M. Utriainen and R. L. Puurunen,



- Saturation profile based conformality analysis for atomic layer deposition: aluminum oxide in lateral high-aspect-ratio channels, *Phys. Chem. Chem. Phys.*, 2020, **22**, 23107–23120.
- 79 J. Dendooven, M. Van Daele, E. Solano, R. K. Ramachandran, M. M. Minjauw, A. Resta, A. Vlad, Y. Garreau, A. Coati and G. Portale, *et al.*, Surface mobility and impact of precursor dosing during atomic layer deposition of platinum: in situ monitoring of nucleation and island growth, *Phys. Chem. Chem. Phys.*, 2020, **22**, 24917–24933.
- 80 J. Dendooven, R. K. Ramachandran, K. Devloo-Casier, G. Rempelberg, M. Filez, H. Poelman, G. B. Marin, E. Fonda and C. Detavernier, Low-temperature atomic layer deposition of platinum using (methylcyclopentadienyl) trimethylplatinum and ozone, *J. Phys. Chem. C*, 2013, **117**, 20557–20561.
- 81 P. Shrestha, D. Gu, N. Tran, K. Tapily, H. Baumgart and G. Namkoong, Investigation of Volmer-Weber growth during the nucleation phase of ALD platinum thin films and template based platinum nanotubes, *ECS Trans.*, 2010, **33**, 127.
- 82 J. Li, B. Zhang, Y. Chen, J. Zhang, H. Yang, J. Zhang, X. Lu, G. Li and Y. Qin, Styrene hydrogenation performance of Pt nanoparticles with controlled size prepared by atomic layer deposition, *Catal. Sci. Technol.*, 2015, **5**, 4218–4223.
- 83 A. Lubers, A. Drake, D. Ludlow and A. Weimer, Electrochemical hydrogen pumping using a platinum catalyst made in a fluidized bed via atomic layer deposition, *Powder Technol.*, 2016, **296**, 72–78.
- 84 H. Van Bui, A. P. Nguyen, M. D. Dang, T. D. Dinh, P. J. Kooyman and J. R. Van Ommen, What could be the low-temperature limit of atomic layer deposition of platinum using MeCpPtMe<sub>3</sub> and oxygen?, *Chem. Commun.*, 2024, **60**, 14045–14048.
- 85 X. Liang, Y. Zhou, J. Li and A. W. Weimer, Reaction mechanism studies for platinum nanoparticle growth by atomic layer deposition, *J. Nanopart. Res.*, 2011, **13**, 3781–3788.
- 86 A. J. Mackus, M. A. Verheijen, N. Leick, A. A. Bol and W. M. Kessels, Influence of oxygen exposure on the nucleation of platinum atomic layer deposition: consequences for film growth, nanopatterning, and nanoparticle synthesis, *Chem. Mater.*, 2013, **25**, 1905–1911.
- 87 F. Grillo, H. Van Bui, J. A. Moulijn, M. T. Kreutzer and J. R. Van Ommen, Understanding and controlling the aggregative growth of platinum nanoparticles in atomic layer deposition: An avenue to size selection, *J. Phys. Chem. Lett.*, 2017, **8**, 975–983.
- 88 S. M. Geyer, R. Methaapanon, R. Johnson, S. Brennan, M. F. Toney, B. Clemens and S. Bent, Structural evolution of platinum thin films grown by atomic layer deposition, *J. Appl. Phys.*, 2014, **116**, 064905.
- 89 A. J. Gayle, Z. J. Berquist, Y. Chen, A. J. Hill, J. Y. Hoffman, A. R. Bielinski, A. Lenert and N. P. Dasgupta, Tunable atomic layer deposition into ultra-high-aspect-ratio (> 60000: 1) aerogel monoliths enabled by transport modeling, *Chem. Mater.*, 2021, **33**, 5572–5583.
- 90 V. A. Vogt, A. J. Gayle, A. Miranda Mañón, A. Lenert and N. P. Dasgupta, Modeling diffusion and depletion in high-aspect-ratio atomic layer deposition processes: Process parameters and manufacturing impacts, *J. Vac. Sci. Technol., A*, 2025, **43**, 062401.
- 91 J. A. Moulijn, J. R. van Ommen, A. Goulas, D. Valdesueiro, J. Juan-Alcañiz, K.-M. Au-Yeung, L. Woning and J. A. Bergwerff, Synthesis of highly-uniform titania overcoats on a mesoporous alumina catalyst support by atomic layer deposition and their application in hydroprocessing, *Catal. Sci. Technol.*, 2023, **13**, 3537–3544.

